Kovove Mater. 64 2026 45–59
DOI: 10.31577/km.2026.1.45

Assessing the performance of CSZ and Al_2O_3-TiO_2 thermal barrier coatings for high temperature applications

Dinesh Diwakar*[1], Vasumathi Manivachakan[1], Saravana Kumar Murugesan[2], Rashia Begum Syed[1]

[1] *Department of Mechanical Engineering, College of Engineering, Guindy, Anna University, Chennai 600025, Tamil Nādu, India*
[2] *Graduate Institute of Manufacturing Technology, National Taipei University of Technology, Taipei 10608, Taiwan*

Received 23 July 2025, received in revised form 5 March 2026, accepted 18 May 2026

Abstract

Super alloys are high-performing alloys used in gas turbine components that are exposed to high temperatures and pressures. When alloys are exposed to temperatures beyond the operating limit of turbines, the material fails. To avoid such a failure, a thermal barrier coating is provided on the substrate. In this work, a single-layer coating of CeO_2 doped with YSZ in the proportion of 1 : 3 percentage is applied on Inconel X750 using the air plasma spray technique. Additionally, a double-layer coating of CSZ as the first layer and, Al_2O_3-TiO_2 as the second layer in the proportion of 3 : 2, is applied on another Inconel sample by the same process. The presence of bond coat and ceramic top coat on the substrate are confirmed by the SEM images. It is perceived from the investigations that, the porosity of the single CSZ layer is more compared to that of the double-layer (CSZ-Al_2O_3-TiO_2) coating. The XRD analysis of the CSZ sample shows the phase transformation of monoclinic to tetragonal ZrO_2 and that of double-layer coating (CSZ-Al_2O_3-TiO_2) shows the transformation of alumina. Raman spectroscopy is done to ascertain the states of various oxides present in the coatings. The double-layer coating exhibits more hardness when compared to the single – layer coating. The hot corrosion test is carried out for 50 hours for both single and double-layer coating in the medium of the mixture containing 25% NaCl and 75% Na_2SO_4 solution. The change in mass per unit area of the CSZ single layer coated sample is more compared to that of CSZ-Al_2O_3-TiO_2 double layer coating.

K e y w o r d s: Thermal Barrier Coatings (TBC), ceria doped YSZ, alumina, titania, hot corrosion, air plasma spraying

1. Introduction

In this modern era, there is an increasing demand for energy, and as a result, thermal systems are being developed to operate at higher temperatures to improve efficiency and output. These high-temperature systems often include gas turbines, steam turbines, nuclear reactors, and various other industrial devices. However, operating at higher temperatures poses significant challenges to the materials used in these systems. [1]. A gas turbine is a combustion-based device that has been used for many years in the fields of mechanical drive, power generation, aviation, and so on [2]. Gas turbine blades and combustion chambers that are subjected to high temperatures are made of nickel-based superalloys that resist corrosion and oxidation. However, prolonged exposure to a high-temperature environment causes materials to degrade, which in turn impairs their mechanical properties and ultimately results in component failure [3, 4].

Thermal barrier coatings (TBCs) are essential for improving the mechanical and thermal performance of parts subjected to high temperatures, especially in the power generation, automotive, and aerospace sectors. By acting as insulating layers, these coatings greatly lower the heat load that is transferred to the metallic

*Corresponding author: tel.: +918526024625; e-mail address: dinesh.diwahar@gmail.com
This article is distributed under the terms of the Creative Commons Attri-bution-NonCommercial 4.0 International Public License (CC BY-NC 4.0).

substrates underneath, enhancing the longevity and effectiveness of high-temperature systems [5–8]. Thermal Barrier coatings (TBCs) are often applied to superalloys. TBCs are made up of two major layers: a metallic bond coat and a ceramic top coat. The ceramic top coats serve as an insulator, offering thermal resistance and shielding the underlying substrate from extreme heat. The component's surface temperature is lowered by this layer's ability to endure intense heat and keep it from transferring it to the substrate. A layer of defense against corrosion and oxidation is provided by the metallic bond coat. The commonly used bond coat is NiCrAlY, which helps to prevent the underlying material, often a superalloy, from undergoing degradation due to exposure to harsh environments [9]. Yttria-stabilized zirconia is the most preferred ceramic top coat; however, it fails because of its lower thermal conductivity at high operating temperatures. Chen et al. [10] observed that when YSZ coatings are exposed to elevated temperatures, decompose and transform into high yttria and low yttria phases. On cooling, it changes its phase to monoclinic, and when it changes to monoclinic its volume gets increased, which eventually leads to catastrophic failure of thermal barrier coatings. Ceria possesses a high thermal expansion coefficient and lower thermal conductivity when compared to YSZ. Therefore, ceria is added to YSZ for improving the thermal shock resistance. Ceria-doped YSZ shows resistance against hot corrosion in the presence of Na_2SO_4 (sodium sulfate) and V_2O_5 (vanadium pentoxide) [11]. Yueh-Cheng and David [12] used silicates and zirconate thermal barrier coatings to prevent delamination and crack penetration in high-temperature superalloys at elevated temperatures. These coatings could improve performance and durability in high-temperature environments, reduce heat transfer, and protect against corrosion and oxidation. Thermally Grown Oxide (TGO) is produced on the top coat when it is oxidized at high temperatures. Because of oxidation, TGO growth at higher temperatures causes spallation. The growth of TGO can cause thermal co-efficient mismatch between the layers as a result of which residual stress is induced in the TGO. Therefore, the formation of TGO growth should be prevented. The material is coated on the substrate using different techniques. It includes thermal spraying, Electron Beam Physical Vapor Deposition (EB-PVD), Air Plasma Spraying (APS), High-Velocity Oxygen Fuel (HVOF), Chemical Vapor Deposition (CVD), etc. The main drawback of using the air plasma spraying is that it reduces the insulation properties [13]. Plasma-sprayed coatings, like YSZ/Al_2O_3, dispersed NiCrAlY on casting and forged Inconel 718 super-alloy have shown promising results in protecting the material from high-temperature oxidation and sulfidation. In the thermal spray process, the coating materials are melted and sprayed on the cleaned surface area of the substrate at high speed. The coating thickness can be varied from several millimeters to micrometers. Plasma spraying [14] is the most familiar technique for thermal barrier coatings. A high-frequency arc is generated between the anode (copper) and the cathode (tungsten). The plasma is generated with a temperature range of 16000 K. Since Ceria-Stabilized Zirconia (CSZ) has a larger thermal expansion coefficient and a lower thermal conductivity than Yttrium-Stabilized Zirconia (YSZ), CSZ-based TBCs have been thoroughly researched as YSZ substitutes. Although CSZ possesses better thermal properties, it has low fracture toughness and high porosity. The hardness of the ceria is decreased due to the addition of YSZ, meanwhile the addition of Al_2O_3 and TiO_2 to the CSZ increases the hardness of the coatings [15]. The nickel based super alloys at high temperature undergo corrosion near the grain boundaries and local stress concentration leads to failure of the coating. The formation of Na_2SO_4 is mainly due to the combustion of sulphur metal impurities present in the fuel or air. During the combustion of gas, NaCl reacts with sulphur dioxide and oxygen forms Na_2SO_4. The alkali in the fuel or air during combustion increases the quantities of sodium and potassium. Vanadium is an unavoidable contaminant in certain liquid fuels and when the components are exposed to high temperature, vanadium deposits cover the components and accelerate the hot corrosion. Vanadium exists at a temperature as low as 535 ℃. The corrosion rate of the substrate can be brought down by using corrosion resistant alloys & multi-layered TBCs and also by reducing the sulphur content in the fuel [16]. Conventional TBC systems are predominantly based on Yttria-Stabilized Zirconia (YSZ); however, concerns regarding phase instability and sintering at temperatures exceeding 1200 ℃ have prompted the exploration of alternative ceramic materials. Among these, Ceria Stabilized Zirconia (CSZ) has emerged as a promising candidate due to its lower thermal conductivity, higher oxygen ion conductivity, and better phase stability under thermal cycling conditions. On the other hand, Al_2O_3-TiO_2 composite coatings are widely known for their superior wear resistance, high hardness, and good adhesion properties, making them suitable for multifunctional protection in harsh environments.

The aim of this work focuses on the enhancement of the life span and reliability of the Inconel X750 substrate under high temperature applications by providing rare earth co-doped Yttrium stabilized zirconia and alumina-titania coatings by the air plasma spraying method. Based on the literature survey, it was confirmed that there was a lack of hot corrosion studies. Hence, this study focuses on investigating the single-layer coating of CeO_2 doped with YSZ in the ratio of 1:3 and double-layer coating of Al_2O_3-TiO_2 in the

Table 1. Inconel X750 chemical composition (wt.%)

Ni	Cr	Fe	Mn	C	Cu
71.20	16.90	5.42	0.12	0.07	0.063
Si	S	Co	Al	Ti	Mo
0.11	0.0028	0.70	0.12	2.53	2.98

Table 2. Thermo physical properties of coating material

Material	Density ($kg\,m^{-3}$)	Specific heat ($J\,kg^{-1}\,K^{-1}$)	Thermal conductivity ($W\,m^{-1}\,K^{-1}$)
Inconel X750	8303	431	15
NiCrAlY	6900	425	12
CSZ	5280	640	1.8
Al_2O_3 + TiO_2	4230	685	22

proportion of 3:2, on an Inconel X750 substrate, using the air plasma spray technique for gas turbine application. The coated samples are assessed for the coating material through SEM, and EDAX studies to ensure the presence of elements in the coating. Vickers micro hardness is evaluated for both the samples. Hot corrosion test is carried out for both the samples in the presence of molten salt environment with 25% NaCl and 75% Na_2SO_4 medium. The surface morphology of the corroded samples is discussed through SEM and EDAX and kinetics of corrosion is studied to assess the mass loss.

2. Materials and methods

2.1 Inconel X750 substrate material

Commercially available Inconel X750 with a diameter of 20 mm and length of 100 mm is chosen as a substrate material for thermal barrier coatings and its composition is mentioned in Table 1. Overall, Inconel X750 is a popular choice for applications that require high strength, and corrosion resistance. Its excellent properties make it a versatile material that is used in a wide range of industries, including aerospace, defense, and power generation.

2.2. Coating material

The bond coat considered in this study is NiCrAlY and the coating material which is used as the top coat in thermal barrier coatings is Ceria (CeO_2) co-doped with Yttrium Stabilized Zirconia (YSZ) and alumina (Al_2O_3)-titania (TiO_2) coating, fabricated

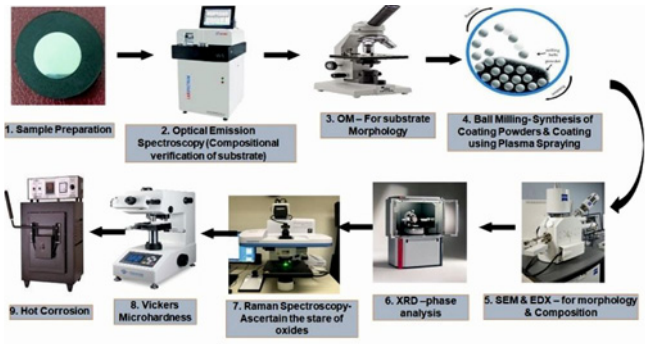

Fig. 1. Development of coating on Inconel X 750 for gas turbine applications.

using the air plasma spraying method. The thermo-physical properties of the coating material are tabulated in Table 2.

2.3. Methodology

The development of coating involves various steps which start from sample preparation, modelling of coating thickness using simulation and process of coating on the Inconel substrate using the air plasma spray technique. After coating, characterizations such as SEM, EDAX, XRD, and Raman Spectroscopy are conducted to ensure the presence of proper coating on the substrate. The hot corrosion test is performed to study the corrosion kinetics of the corroded sample. The development of coating on Inconel X750 is carried out for gas turbine application and the methodology is explained through Fig. 1.

2.3.1. Sample preparation

An Inconel X750 Alloy Specimen is cut into a thickness of 4 mm and diameter of 20 mm using Wire Cut Electric Discharge Machining (EDM). Then the sample is molded and polished with 1000, 1500, and 2000 grades of Emery Sheet. The final Polishing is done using a Velvet cloth disc machine.

2.3.2. Optical emission microscopy

An Inconel X750 Specimen Composition analysis is done using Optical Emission Spectroscopy (OES). It is a widely used analytical technique to determine the elemental composition of a broad range of metals. It generates a spark between an electrode and a metal sample, then the vaporized atoms are brought to a state of high energy. These excited atoms produce characteristic emission spectral lines. The wave-length emitted is characteristic of the chemical element. The detectors measure the intensity of the spectrum of each element. The intensity of each emission

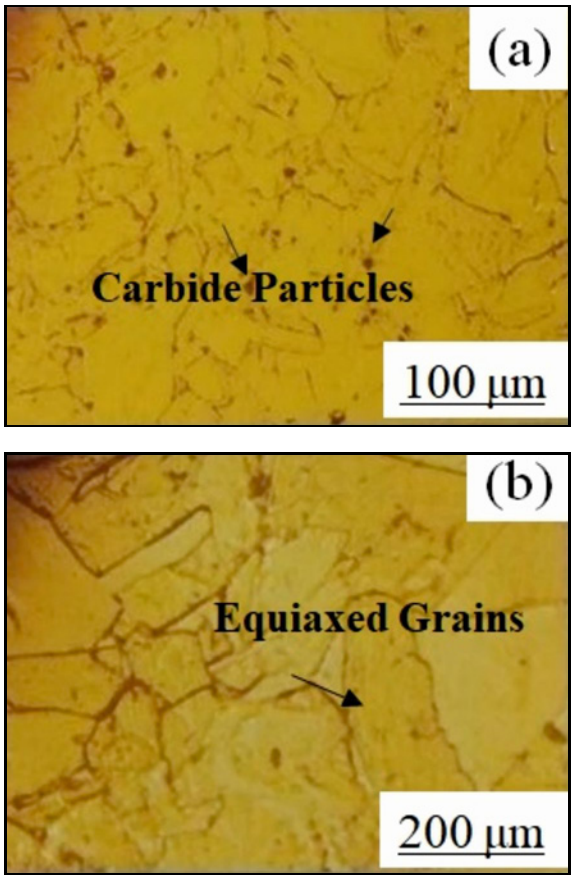

Fig. 2. Optical Microscopic Image of Inconel X750 (a) 200× and (b) 500×

spectrum depends on the concentration of the element in the sample. This microscopic analysis ensures the existence of the composition of the Inconel X750 sample as mentioned in Table 1.

2.3.3. Optical microscopy of Inconel X-750 substrate

The metallography of the prepared Inconel X750 samples (substrate) is analyzed using Optical Microscopy. The samples are etched with Kalling's 1 reagent (5g copper chloride, 100 mL hydrochloric acid, 100 mL alcohol, and 100 mL water) and observed for carbide particles and grains present in the sample. The specimens are viewed at a magnification of 200× and 500×. The microstructure can be somewhat complex because of various phase transformations happening due to the incorporation of precipitation hardening. In Fig. 2a, the grains are distributed uniformly in an equiaxed form. It is also observed that there are no uncrystallized grains that are fully replaced by recrystallized grains. It also contains some carbide particles and is distributed in a random manner in the gamma matrix as shown in Fig. 2b. The specimen reveals clear grain boundaries that are devoid of carbide segregation at grain boundaries as observed in the case of Hong et al. [17].

2.3.4. Synthesis of Coating Powders

The NiCrAlY (Ni-20.0-26.0; Cr-11.0-14.0; Al-0.1-0.8; Y-0.1-0.7 (wt.%)) powder (Amdry 365-1, Oerlikon Metco, nominal composition) that is available in the market is gas-atomized. The coating powder NiCrAlY with spheroidal morphology and particle size ranging from 5 to 45 µm is employed as the bond coat material. Commercial feedstock of Ceria (CeO_2), YSZ, Al_2O_3, and TiO_2 acquired from Sigma Aldrich which is 99.99% pure, is used as the top coat. The plasma spray grade Cerium Oxide and Yttria Oxide, Zirconia, Alumina, Titania, is selected with a particle size less than 30–45 µm, in order to facilitate easy spraying in the plasma spray equipment. Planetary ball milling device at room temperature is used to mechanically grind the coating powder at compositions of 25 wt.% CeO_2, 75 wt.% YSZ 60 wt.% Al_2O_3, and 40 wt.% TiO_2. The ball (with size of 10 mm) made of AISI 52100 hardened steel vials, each of 250 ml capacity, is used in the milling treatment, for a period of 12 hours. The argon atmosphere used is 99.99% pure.

2.3.5. Modelling of coating thickness using simulation

In order to forecast the coating thickness on the substrate, computational and numerical approaches are used in the modelling of coating thickness. Knowing how factors such as coating material qualities, application methods, and environmental factors impact the final coating thickness requires a grasp of this process. When the coating thickness on a blade is infinitely small in comparison to the blade diameters in other directions, the 2D-plane model of the cross-section of the blade is employed, and the boundary conditions for heat conduction and convection are taken to be in the direction of the coating thickness. The two dimensional, 4 noded quadrangle solid element PLANE55 is selected for analysis in the code ANSYS APDL module. The top ceramic layer (TC1), interior ceramic layer (TC2), and bond coat (BC) layer, substrate are the four layers that make up the numerical model, which is based on the Double Coat Layer (DCL)-TBC arrangement as shown in Fig. 3a. The thickness of the bond coat is chosen as 100 µm, and the thickness of the substrate layer is chosen as 4 mm. The assumptions taken into consideration are that the layers are homogeneous and isotropic in nature, and that the left and right sides of the model are considered as adiabatic boundaries [18]. The temperature of the high-temperature gas is set as 1500 K and its heat transfer coefficient is

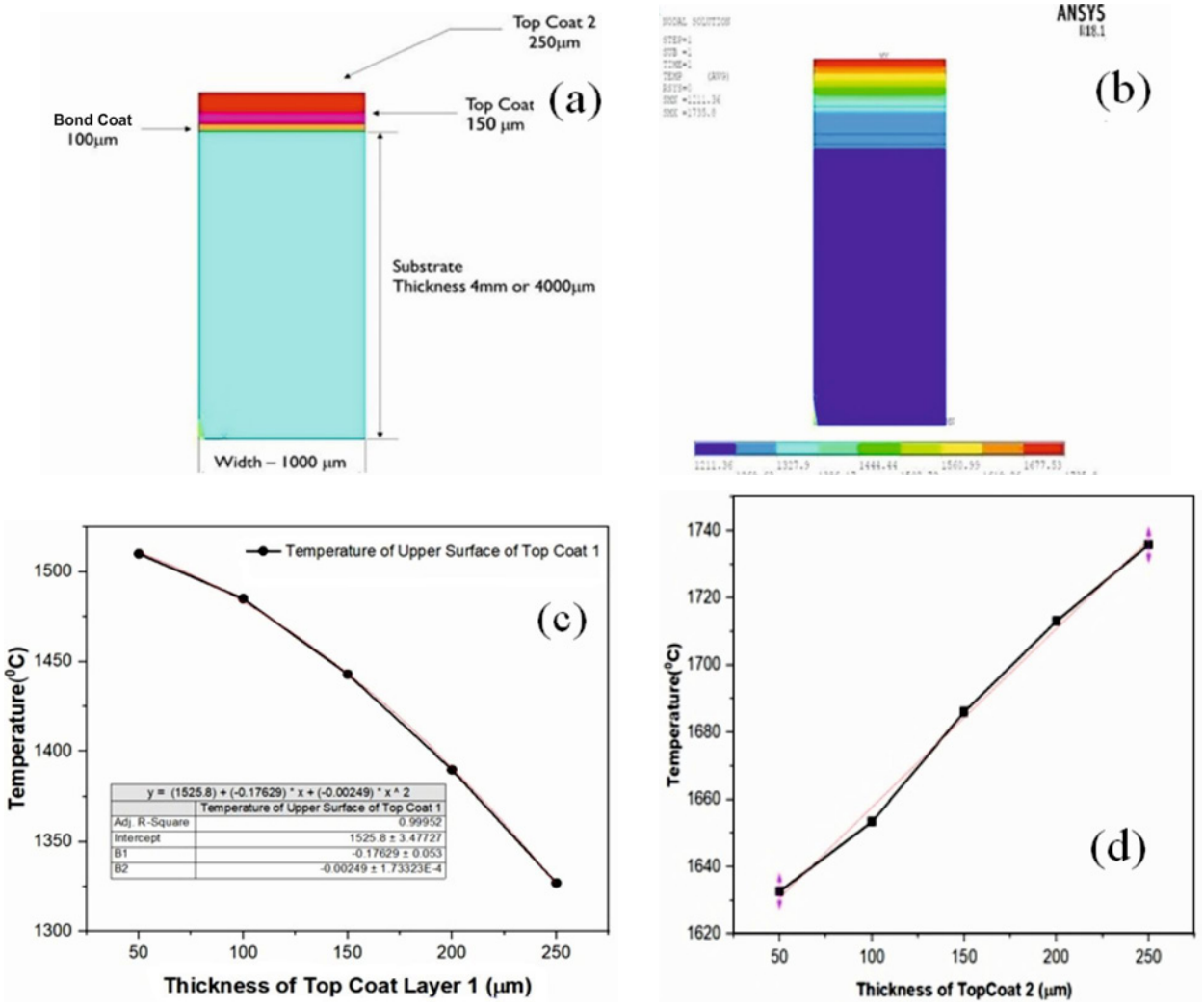

Fig. 3. (a) Finite element modelling of double-layer TBC, (b) temperature distribution of the DCL-TBC variation of the temperature of the upper surface of the (c) TC1 & (d) TC2 layer.

2500 W m^{-2} K^{-1}. The temperature of the cooling gas is 1000 K, and the heat transfer coefficient on the cooling side is 2750 W m^{-2} K^{-1}. The initial temperature of the model is set as 250 K [19–21]. The thermophysical parameters of the materials of the four layers (TC1, TC2, BC, and substrate) in the DCL-TBC system are listed in Table 2. Based on the physical mode and three kinds of mechanism of heat transfer, a numerical model has been developed using a finite element package code.

By keeping the thickness of the first Top Coat (TC1) layer constant and by changing the thickness of the second Top Layer (TC2), the change in the temperature of each layer in the DCL-TBC is obtained. The temperature distribution in the Double Coated Layer-Thermal Barrier Coating (DCL-TBC) system is displayed in Fig. 3b, for Top Coat 1 with a thickness of 150 μm and Top Coat 2 with a thickness of 250 μm. The thickness of the first top layer is set as 150 μm and the thickness of the second layer (TC2) is chosen in the range of 50 to 250 μm. From Fig. 3d, it is evident that the temperature of the Top coat 2 upper surface increases linearly. Likewise, by keeping the thickness of the second top (TC2) layer constant and varying the thickness of the TC1 layer, variations in the temperature of each of these layers in the DCL-TBC can be found. From those variations, it can be seen that the temperature of the top coat 1 upper surface decreases linearly which is apparent from Fig. 3c. The thickness of TC1 (HTC1) and total coating thickness (H total) are treated as independent variables. Specifically, the values of HTC1 are chosen in the range from 0 to 200 μm, and the values of H total are chosen in the range from 200 to 400 μm. These two parameters are considered as data points in a matrix of the HTC1-H total. The results (the temperatures of each layer) can be processed and displayed by the 2D contour map of the HTC1-H total temperature of layer (TC1 & TC2) using the *Python program*. Since the sintering temperature of each layer is typically lower than the

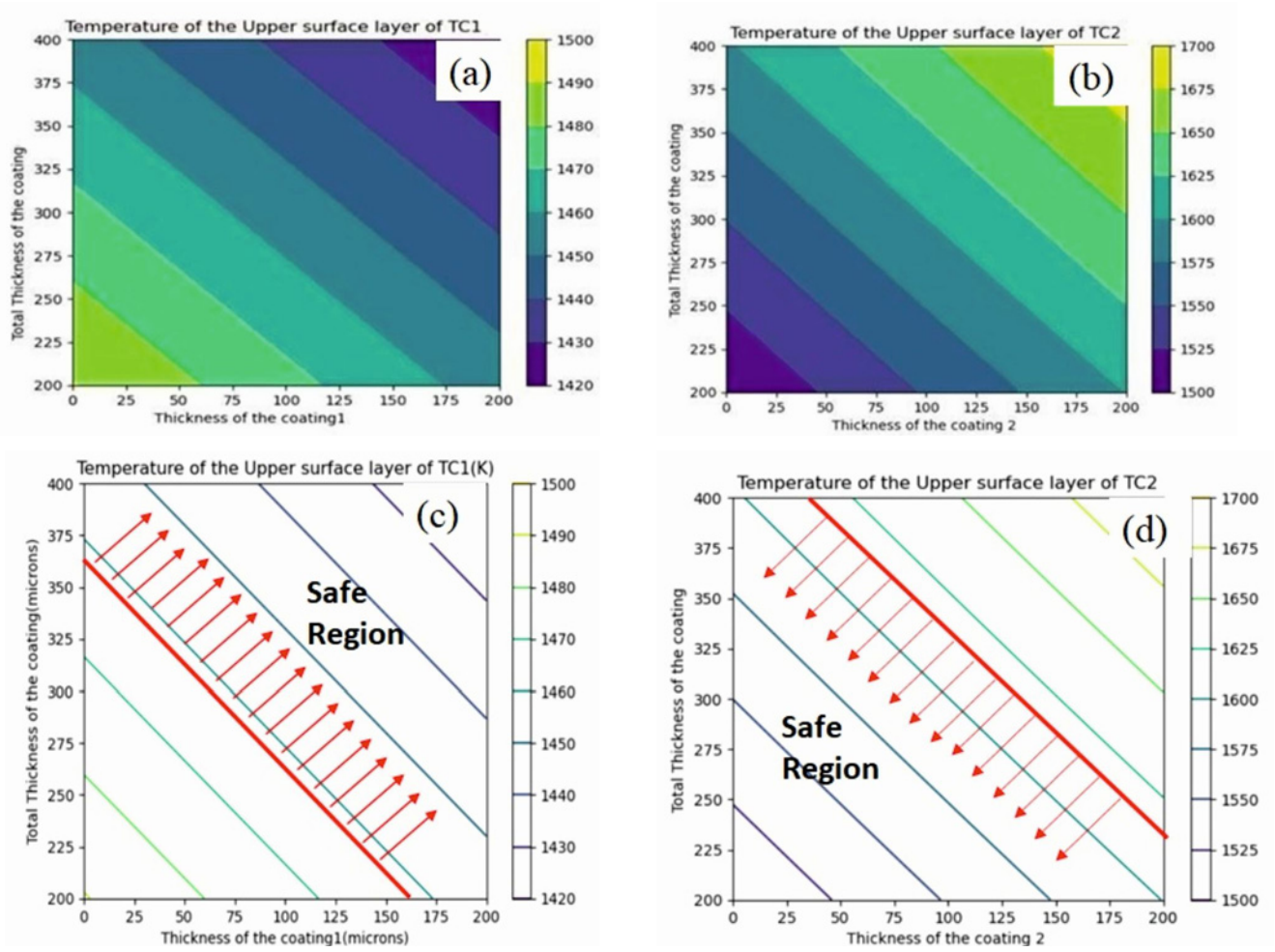

Fig. 4. Contour map of HTC1-*H* total-temperature of upper surface of (a) TC1 & (b) TC2 layer, plot for HTC1-*H* total-temperature of upper surface of (c) TC1 & (d) TC2.

phase transition or melting point temperature, it is fair to use the sintering temperature as an acceptable parameter to assess the thermal safety of each layer [22]. The sintering temperature of every layer is indicated on the contour map as shown in Figs. 4a,b. As seen in Fig. 4c, the thickness of the Top layer 1 is selected from the safe area of the contour plot, with the sintering temperature of 1423 K. With the use of the sintering temperature criterion, the safety of the second top layer is assessed. The safe plot for Top Coat 2 layer is shown in Fig. 4d, and the sintering temperature of Top Layer 2 is found to be 1630 K.

2.3.6. Plasma spraying process

The plasma spraying process is carried out by Plasma Technik AG; Switzerland F4-MB gun (Sulzer-Metco; Switzerland, 2012) in the air medium at Spraymet Surface Engineering Pvt Ltd, Bangalore. The parameters for the spray coating process are mentioned in Table 3. For the purpose of enhancing the adhesion of the substrate, and to remove the impurities it is grit blasted with alumina. Two samples of Inconel X750 substrate of diameter 20 and 4 mm thickness are used for plasma spraying, a bond coat of

Table 3. Parameters for plasma spraying process

Process parameters	Specification
Powder feed rate ($g\,min^{-1}$)	40–45
Plasma current (Amps)	900
Torch power input (KW)	40
Primary gas (Argon) in LPM	80–90
Powder size (μm)	35–45
Carrier gas (Hydrogen), LPM	16–18
Voltage (V)	65
Current (Amps)	500
Powder speed ($m\,s^{-1}$)	200
Stand-off-distance (mm)	80
Spray angle (°)	90

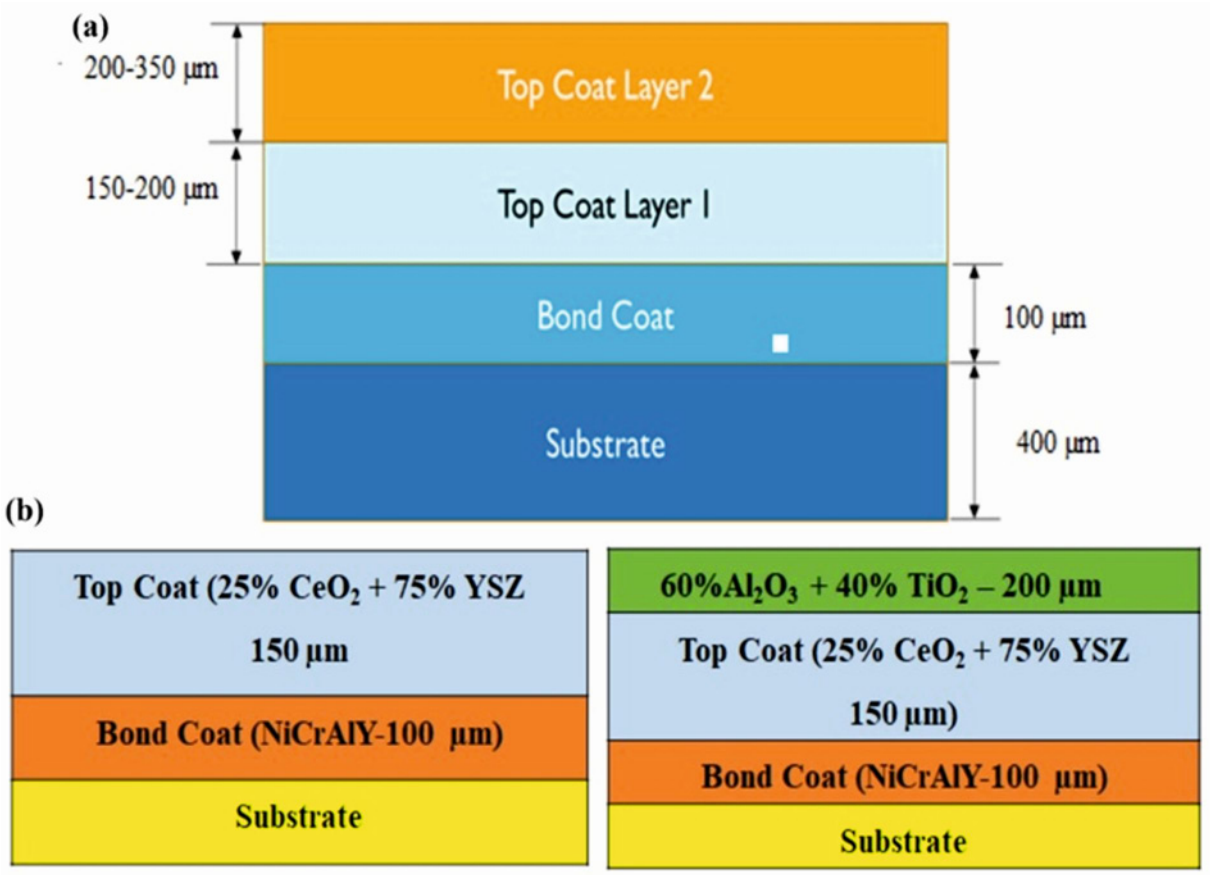

Fig. 5. (a) Proposed coating thickness for fabrication of coating on Inconel X750 substrate and (b) composition.

NiCrAlY of 100 µm thickness and a top coat of composition (75 wt.% YSZ + 25 wt.% CeO_2) is sprayed on the first sample with the thickness of 150 µm and the second sample with double layer coating of (75 wt.% YSZ + 25 wt.% CeO_2) and (40 wt.% TiO_2 + 60 wt.% Al_2O_3) with the total coating thickness of 350 µm (excluding Bond coat thickness) as shown in Figs. 5a,b. The thickness of the coating can be ensured by using coat PCE-CT27 thickness gauge. The porosity of the first sample is more and to overcome the porosity of the first sample, 60 % alumina and 40 % titania is added additionally as the second layer, confirmed using the SEM analysis.

2.3.7. Characterization of coating

The Scanning Electron Microscope (SEM) is used to illustrate the morphology of CSZ coating and CSZ-Al_2O_3-TiO_2 coatings on Inconel X750 sample. Energy Dispersive Spectroscopy is used to analyze the elemental presence. The elemental mapping shows the dissemination of elements in the coating. The phase identification could be done by using X-Ray Diffraction (XRD). Raman spectroscopy is carried out to ascertain the state of oxides and it provides the chemical information about the coatings.

2.3.8. Mechanical testing of the coated samples

The hot corrosion behavior can be studied as per ASTM G41 standards on the circular samples in order to avoid the thermal stress around the sharp corners to avoid spallation. The porosity of the coated samples can be found by using Scanning Electron Microscopy (SEM) interfaced with the image analyzer software. The Vickers micro-hardness is conducted as per ASTM E384 to assess the hardness of the coated samples. The thickness of the coating can be ensured by using PCE-CT27 thickness gauge.

3. Results and discussions

3.1. SEM analysis of the thermal barrier coated sample

The morphology of the coated samples is analyzed using Scanning Electron Microscopy (SEM) for the formation of bond coat (NiCrAlY) and top coat (CSZ), layers on the Inconel X 750 substrate. From Fig. 6b, it can be clearly seen that pores, cracks, discontinuous openings and unmelted particles are avail-

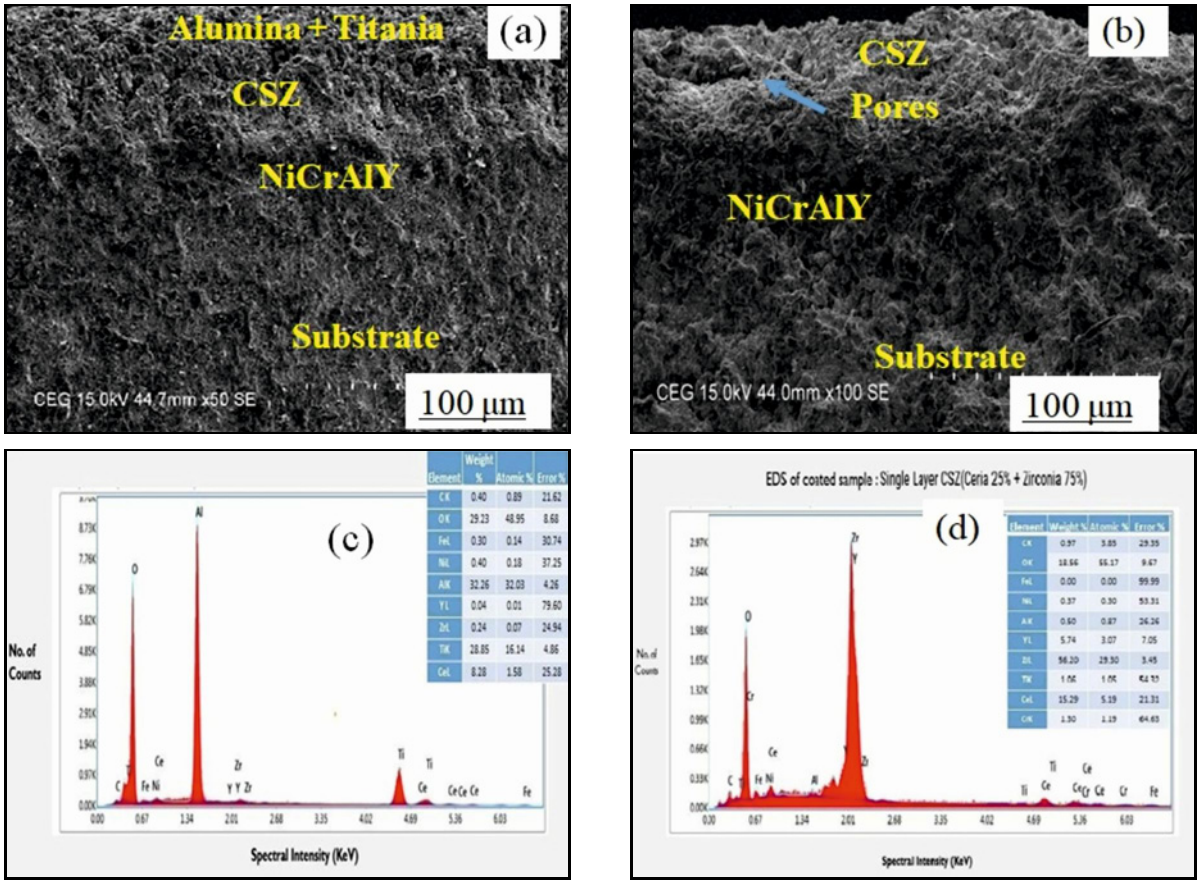

Fig. 6. (a) SEM Morphology of CSZ-Al_2O_3-TiO_2, (b) SEM morphology of CSZ, (c) EDS spectra of CSZ-Al_2O_3-TiO_2 coated sample, and (d) EDS spectra of CSZ coated sample.

able on the ceramic top coating. The Double Layer coating of CSZ-Al_2O_3-TiO_2 thermal barrier coating is illustrated in Fig. 6a. The double layer coating exhibits a smaller number of pores and cracks and also exhibits a rough surface. A greater number of pores is observed on the CSZ sample compared to the CSZ--Al_2O_3-TiO_2 sample. The coatings are well adhered to the surface and no visible cracks are observed on the surface of the sample. Lattice conduction is the main mechanism for the materials that do not contain free electrons, such as ceramics (YSZ) which depend upon temperature and scattering of photons by geometric defects. Due to the limited thermal conductivity of air or gas in pores, photons at high temperatures help in the conduction of heat via the pores. In general, the TBC structure has a particular number of pores and cracks that lowers its heat conductivity and increases its thermal shock resistance as observed by Vargas et al. for Inconel 718 sample [23].

3.2. EDS Analysis

The EDS spectra of the Single Layer CSZ (ceria 25 % + zirconia 75 %) has been analyzed using Energy Dispersive Spectroscopy displayed in Fig. 6d. The CSZ coated layer contain the elements of ceria, zirconia, carbon, oxygen, nickel, aluminum, iron, and yttrium. The EDS spectrum illustrated from the graph shown that, the intensity of peaks is high for the main composition of zirconia and yttrium. The intensity of X-Ray peaks corresponds to elemental composition and concentration of elements in CSZ.

The EDS spectra of double Layer (CSZ & mixture of alumina and titania) have been shown in Fig. 6c. It is evident from the graph that the intensity of peaks is high for the main composition of alumina & titania. The elemental mapping ensures the presence of double layer coated elements. By comparing the X-ray peaks with known standards, quantitative analysis is performed to determine the relative amounts of different elements in the coating. The distribution of elements is homogeneous on the coated surface and this indicates proper application of coating throughout the process.

3.3. X-Ray diffraction (phase analysis)

The XRD pattern of Inconel X750 for the CSZ sample (25 % CeO_2 + 75 % YSZ) is demonstrated through Fig. 7a and the formation of elements is confirmed with the help of standard JCPDS Pow-

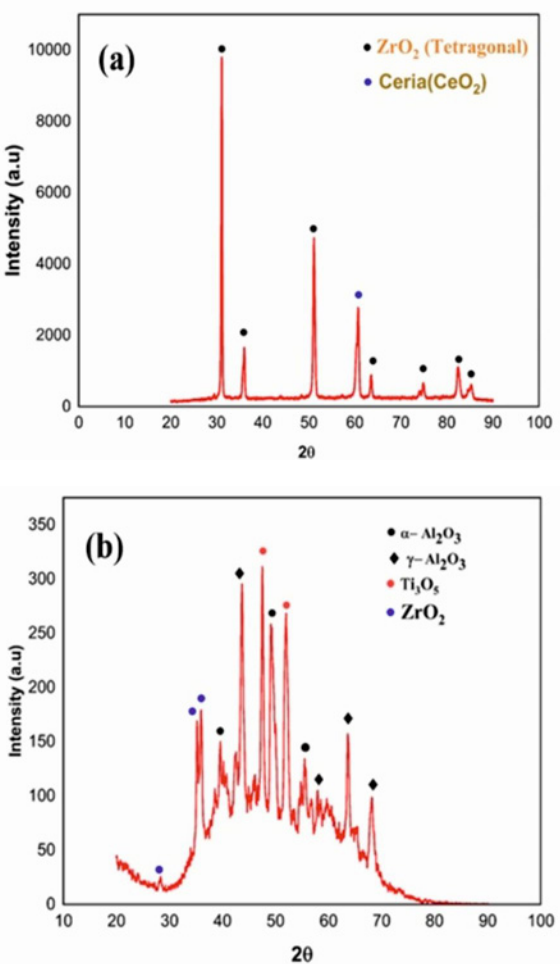

Fig. 7. (a) XRD Pattern of CSZ sample and (b) XRD Pattern of CSZ-Al_2O_3-TiO_2 sample.

der Diffraction data. The cubic nature of zirconia is responsible for every diffraction peak; however, the characteristic reflections for the tetragonal and cubic phases have been located. The XRD analysis of the CSZ coated sample shows the presence of ZrO_2 & CeO_2 with (2,0,0) and (2,2,0) XRD pattern. The CSZ consists of tetragonal ZrO_2 (t') phase and CeO_2 as ensured by JCPDS $\neq$ 01-082-1245 and JCPDS $\neq$ 34-0394 files respectively [24]. The broad width of the CSZ phase is due to the presence of refined grain size. The zirconia that is present in the CSZ coating is a non-transformable tetragonal phase. Due to the very fast cooling of molten particles during the plasma spraying process, the plasma sprayed coating does not have an equilibrium structure. The tetragonal phase stabilized by martensitic transformation during quick cooling without generating a monoclinic phase is known as a non-transformable tetragonal (t-prime) phase. Since the thermal expansion coefficient of the t-phase is larger than that of the zirconia phase, it is more resistant to thermal shock on the super alloy substrate [25]. Following the CSZ powder plasma spraying, Park et al. [26] described the occurrence of more than 99 wt.% of tetragonal phase on cooling. Rhombohedral (α) and cubic (γ) phases are present in Al_2O_3 coatings, whereas CSZ lacked a transformable tetragonal (t') phase as in the case of CSZ-Al_2O_3-TiO_2. The XRD pattern of (60 % Al_2O_3 + 40 % TiO_2 + 25 % CeO_2 + 75 % YSZ) shows some of the α-Al_2O_3 and γ-Al_2O_3, ZrO_2 is observed on the top of the coating. It is also noted that the titania (TiO_2) phase is observed in the sample with 40 % TiO_2. The XRD patterns, near the (1,1,3) – α-Al_2O_3 and (4,0,0) γ-Al_2O_3 for alumina-titania coatings are shown in Fig. 7b. It has been recognized that the more the fraction of partially melted particles are, the higher the content of the presence of α phase after plasma spraying. Thus, the increase of α-Al_2O_3 in the nanostructured coating may be relative to the decrease of the melting degree of the substrate [27]. The peaks of TiO_2 have disappeared from the XRD spectrum of coatings. For the conventional coatings, titania is present in the modification of Ti_2O_3 generated from Ti_3O_5 that was deoxidized during the plasma spraying process.

3.4. Raman spectroscopy

Raman spectroscopy can identify the crystalline phases that are present in a material based on the number of bands that are observed and their wave numbers, which are correlated with the space group and the force constants of the bonds, respectively. The Raman spectroscopy is done at room temperature using (LabRAM HR 800, HORIBA JOBIN YVON, and France 2010) equipped with a 2000 × 800-pixel Charge-Coupled Device (CCD) detector (Spex Industries, Edison, NJ). Spectra are recorded in the micro configuration, with the laser beam impacting a region with diameter of 1 μm. To eliminate background noise, baseline correction is used for the spectral arrays. Low collection counts and high relative noise are reported in metal-collected spectra, which has made them unusable for analysis. Hence, for spectral arrays, the convolution of Gaussian and Lorentzian peak fitting is gathered. For several peaks in each spectrum, peak position, amplitude, and Full Width Half Maximum (FWHM) are gathered and organized into X-Y maps. Figure 8b represents the Raman spectra of CSZ, which acquires a wavelength between 109.24–378.36 cm^{-1}. The tensile strain is induced in the thin film of CSZ coating which causes a shift in the position of Raman bands to lower wave, with respect to reference strain free material [28]. Distinct vibrational spectra have been established for both monoclinic and tetragonal zirconia. A tetragonal phase is observed in the CSZ sample at lower temperatures. The large peak of the spectrum corresponds to a fluorite structure and the small one is due to the defect structure that occurred

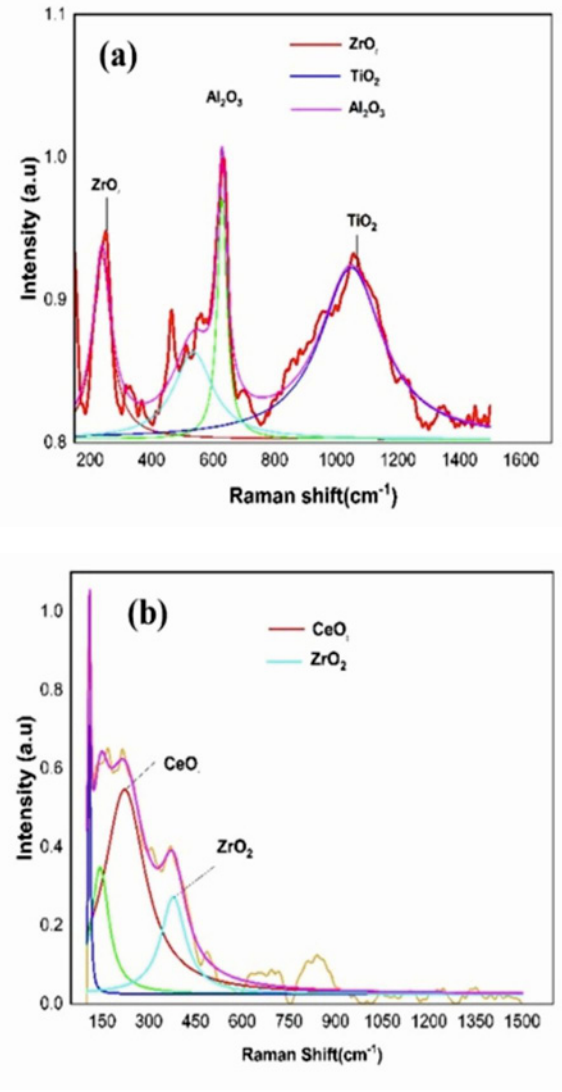

Fig. 8. Raman spectroscopy (a) CSZ-Al_2O_3-TiO_2 sample and (b) CSZ Sample.

as a result of substitution of the zirconium cations by cerium. The band above 378 cm^{-1} in the CSZ sample corresponds to the tetragonal phase, which proves the presence of ZrO_2 and the band above 228 cm^{-1} corresponds to CeO_2, that are similar to the results of Wheeler et al. [29].

The Raman spectra of CSZ-Al_2O_3-TiO_2 as shown in Fig. 8a exhibit a band range of 239–1048 cm^{-1}. The tetragonal phase is observed at the band of 239 cm^{-1} which corresponds to ZrO_2 and (60 % Al_2O_3 + 40 % TiO_2) composition is recorded in the range of 628–1048 cm^{-1} due to reaction formed between Al_2O_3 and TiO_2. The band range formed between Al_2O_3-TiO_2 is not due to vibrational transition. The addition of TiO_2 to Al_2O_3 causes a decrease in the intensity of the Al_2O_3 peaks. The presence of titanium oxide at the surface causes decreases in the Raman signal due to

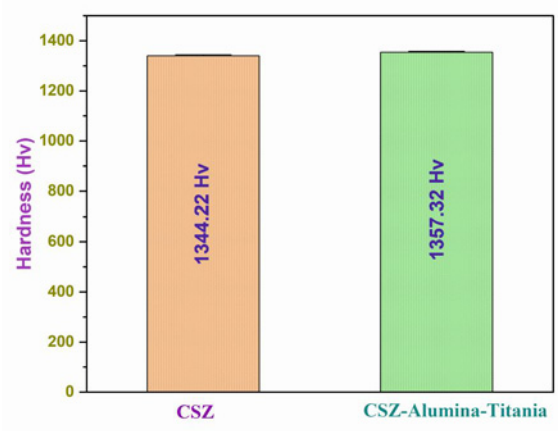

Fig. 9. Hardness comparison of CSZ and CSZ Alumina-Titanium Coating.

alumina fluorescence, which in this case, has appeared at 1048 cm^{-1} as in the case of Luo et al. [30]. These observations fully agree with the XRD data.

3.5. Vickers micro hardness test

The results of the micro hardness test have been expressed as the length of indentation diagonal and it has been carried out by using MT91 series hardness tester [Metek, 2011]. Vickers Micro hardness test is carried out with the load of 500 gf with the dwell time of 30 seconds and unloading time of 15 seconds. The average Vickers hardness for single layer (ceria 25 % and 75 % YSZ) is found to be 1344.22 HV and the average Vickers hardness for the double layered coating (25 % Ceria, 75 % YSZ, 60 % Al_2O_3, and 40 % TiO_2) is observed to be 1357.3 HV as shown in Fig. 9. The values of hardness are represented in Table 4. The hardness value HV of the coated specimen can be calculated by using the Eq. (1):

$$\mathrm{HV} = (1.8544F)d^2, \tag{1}$$

where F is in Kgf and d is in mm.

It is found that the average Vickers microhardness value of double layer coating is more than that of the single layer coating. The bulk hardness of (CSZ-Al_2O_3-TiO_2) coating is higher when compared to that of CSZ coating due to the sintering process. The hardness value increases with an increase in the addition of Al_2O_3-TiO_2 to CSZ which earlier contained a softened layer of the zirconia phase. The lamellar distribution of phases presents in the (CSZ-Al_2O_3-TiO_2) coating reduces the surface defects, thereby increasing the hardness. The sintering process could also affect the distribution of phases during the spraying process [31]. The higher the hardness value, the higher the bonding capacity between the coating and the substrate.

Table 4. Hardness Results of Coated samples

Samples	Average hardness Value (HV)
Ceria 25 % and 75 % YSZ (wt.%)	1344.22
Ceria 25 % 75% YSZ, 60 % Al_2O_3, 40 % TiO_2 (wt.%)	1357.3

The toughness value can be decreased by increasing the hardness. Spallation is one of the major reasons for the failure of the coating. The microcracks were very thin and arrested in the microstructure, hence no cracks were noticed till 200 gf load similar to the results of Hashemi et al. [32].

3.6. Hot corrosion test

In the corrosion studies, the blended salt deposition is used instead of atmospheric air as a medium. In this study, the salt mixture of NaCl and Na_2SO_4 is used. The salt proportion in accordance with a gas turbine environment is used for the study. The hot corrosion test is carried out in a tubular furnace and initially the mass of the coated sample is calculated by using a digital balance. Initially the mass of the sample containing ceria (25 %) and YSZ (75 %) is 10.75 g whereas that of the sample containing ceria (25 %), YSZ (75 %), Al_2O_3, (60 %), and TiO_2 (40 %) is 11.175 g. After the initial mass measurement, the surface area of the sample is calculated. Based on the area exposed to corrosive environment, the salt mixture is prepared. A concentration of 2–3 mg cm^{-2} of the salt mixture containing 25 % of NaCl and 75 % of Na_2SO_4 is applied on each surface of the sample by using a hair brush. The samples are kept in the ceramic boat and preheated to 250 ℃ in the furnace for the purpose of eliminating the moisture contents present in the salt. The hot corrosion studies of the coated samples have been carried out at the temperature of 1200 ℃ for fifty hours with an interval of six hours. The mixed salt environment used and the results are as per the ASTM G41 standard. Circular samples are employed for this analysis in order to avoid the thermal stress accumulated around the sharp corners which may cause spallation at those positions [33].

The mass change of the coated samples is evaluated after the fifty hours of heat treatment. The corroded samples are characterized by using Scanning Electron Microscopy (SEM) and Energy Dispersive X-Ray Spectroscopy (EDS) to study the growth and presence of the components in the coatings. During the corrosion process, spallation of coating occurs and it is represented in Fig. 10a. The main reason for the spallation of the oxide is the growth of intermittent layer. The intermittent layer is nothing but thermally grown oxide layer formed between the substrate and the top coat due prolonged exposure. [34].

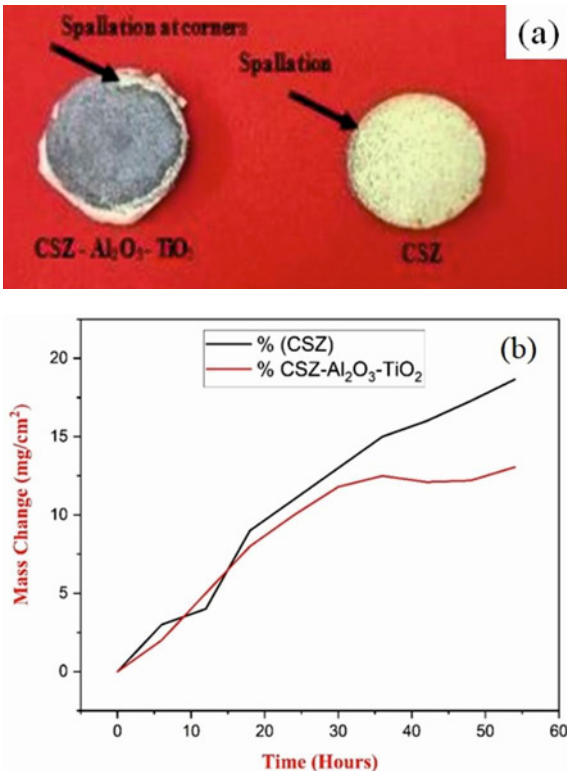

Fig. 10. (a) Hot corrosion samples of CSZ and CSZ alumina-titanium coating and (b) corrosion kinetics of CSZ and CSZ alumina-titanium coating.

3.7. Kinetics of the coated samples exposed to corrosion

To determine the kinetics of the corrosion process, the change in mass with respect to time is assessed. Different growth models (linear, parabolic, or logarithmic law) can be used, however parabolic oxide growth is commonly utilized. The kinetics of corrosion can be evaluated by the growth rate time constant or n-values, through Eq. (2). The mass change with respect to time is given by:

$$\Delta m = Kt^n, \tag{2}$$

where Δm is mass change per unit area (mg cm^{-2}), t is time exposed in hours, K and n are constants, that are not dependent on the material and corrosive

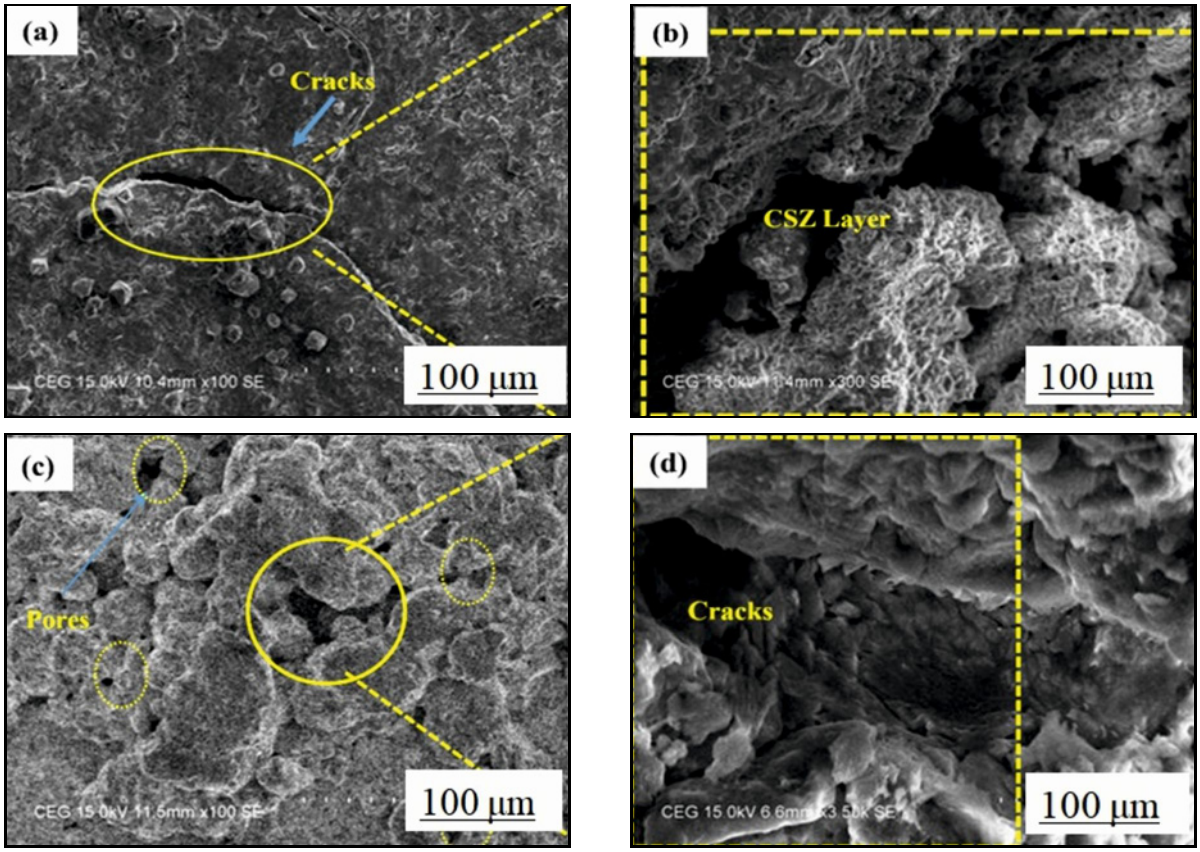

Fig. 11. (a) SEM Image of CSZ-Al_2O_3-TiO_2 sample at 1000 °C, (b) CSZ Al_2O_3-TiO_2 visible crack, (c) morphology of CSZ at 1000 °C, and (d) cracks in CSZ layer.

environment, if the constant $n = 1$, the variation of mass with respect to time is linear and if $n = 2$, it is parabolic in nature and $n = 3$, cubic or logarithmic in nature.

Initially, the mass of the sample containing ceria (25 %) and YSZ (75 %) is 10.75 g and the mass of the sample containing ceria (25 %), YSZ (75 %), Al_2O_3, (60 %), TiO_2 (40 %) is 11.175 g are exposed to a mixture containing NaCl and Na_2SO_4 in the ratio of 1 : 3 at the temperature of 1200 °C, each sample maintained for fifty hours. The samples under molten salt environment show the progressive increase in mass change due to the occurrence of a eutectic reaction existing between the contents of the salt mixture at the exposed temperature. The changes in mass observed in the CSZ sample and CSZ-Al_2O_3-TiO_2 samples are found to be 10.8086 and 11.216 g respectively, therefore the maximum mass change is observed in the CSZ sample. The mass change per unit area of the CSZ sample is 18.66 mg cm^{-2} and for the CSZ-Al_2O_3-TiO_2 sample it is 13.057 mg cm^{-2}. Hot air with invariant mass changes, however, has caused the sample to behave catastrophically. It is because of the uniform phase change happening during the prolonged exposure to high temperatures.

Due to the presence of sulfate and chlorine in samples, it is prone to more corrosion. Mousavi et al. [35] also reported the sequence of hot corrosion attack in super alloy in the presence of sulfate and a combination of sulfate and chloride. From Fig. 12, the corrosion behavior of the coated sample CSZ sample is found to be more and alumina-titania doped CSZ samples is found to undergo less corrosion when compared to that of the CSZ coated samples in molten salt environment. In addition to this, a reduced mass change is observed in the alumina-titania CSZ sample. The mass change in the coated (CSZ-Al_2O_3-TiO_2) Inconel X750 sample is due to presence of aluminium and it is more susceptible towards the high temperature to form oxides as observed in the case of Negati et al. [36]. The corrosion kinetics follows the parabolic law because the mass gain increases as the temperature increases, which is evident from Fig. 10b and also from Eq. (2) for the value of $n = 2$. From Eq (2), the parabolic rate constant, K is calculated and is found to be 1.076×10^{-8} $mg^2\,cm^{-4}\,s^{-1}$ for the CSZ sample and is found to be 5.26×10^{-9} $mg^2\,cm^{-4}\,s^{-1}$ for the CSZ-Al_2O_3-TiO_2 sample. The parabolic rate constant is higher for the CSZ sample compared to that of the CSZ-Al_2O_3-TiO_2 sample. Sometimes the addition of YSZ increases the value of the rate constant.

3.8. SEM Analysis of corroded sample

The SEM morphology of the CSZ-Al_2O_3-TiO_2 sample exposed to NaCl and Na_2SO_4 (25 % + 75 % (wt.%)) salts maintained at 1000 ℃ for fifty hours duration is exposed. Because of prolonged exposure of samples at 1000 ℃ at fifty hours, micro pores have led to the formation of micro cracks and the occurrence of spallation of oxides scale along the sample edges. Groove attack along the splat boundaries is visible, as in Fig. 11a. The CSZ layer has undergone corrosion attack after the crack formation in the edges of Al_2O_3-TiO_2 coated sample which is observed from Fig. 11b. Along with micro cracks, porous coating and un melted particles are also clearly visible in the image. The formation of cracks is attributed to the occurrence of residual stress induced during the deposition process, and because of micro cracks and pores, gas entrapment occurs along the surface of the sample, similar to the works of Shamshini et al. [37].

From Fig. 11c, it is evident that the penetration of molten salts through coating causes the formation of micro cracks and open pores in the CSZ sample. The creation of crack in the sample is due to the formation of stress accumulation during heating and phase transformations of monoclinic ZrO_2 and CeO_2 crystals, as shown in Fig. 11d. The expansion of the volume of the crystal upon cooling, causes the failure of the coating, similar to the results of Shi et al. [38]. The bond coat undergoes oxidation and leads to failure of coating.

3.9. Spectroscopic analysis of corroded samples

Energy dispersive spectroscopy is used analyze the composition of CSZ and CSZ-Al_2O_3-TiO_2 when exposed to molten salt environment at the temperature of 1000 ℃ for fifty hours. The EDS spectra show the element present in the coating as shown in Fig. 12a. The dissolution of titania in the salt medium is less when compared to that of aluminium oxide which is present in the coating as observed from the EDS spectra for the CSZ-Al_2O_3-TiO_2 sample. The amount of sodium and chlorine present in the salt mixture is 29 and 22 %, respectively. Elements such as Na, Cl, Al, Ti, O, and S are identified in the EDS mapping. The EDS spectra of the CSZ sample under molten salt environment at high temperature is shown in Fig. 12b. The spectra reveal that sodium is present in higher proportions under heating in the molten environment. The spectra additionally reveal the percentage of salt content in the coating which is observed to be 22.2 % of sodium and 25.8 % of chlorine and higher amounts of zirconium at 32 %. The elemental spectra for the CSZ sample in the molten environment reveal the presence of elements such as Na, Cl, Ce, Zr, Y, and O. At high temperatures, the CSZ sample corrodes more and more micro cracks are observed on the surface of the sample.

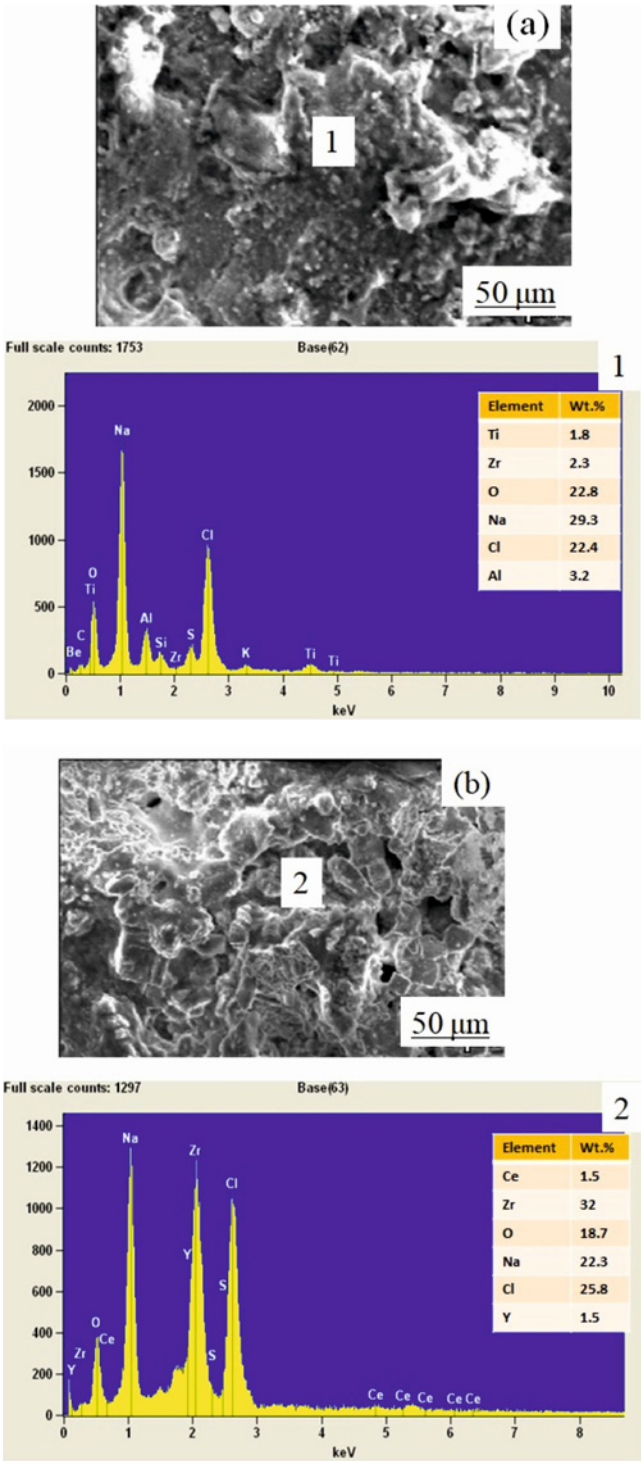

Fig. 12. (a) EDS Analysis of CSZ-Al_2O_3-TiO_2 and (b) CSZ Sample under molten salt environment.

4. Conclusions

In order to improve the shelf life of components subjected to high temperatures, a study has been car-

ried out in this work on an Inconel X750 substrate by coating it with different layers of CSZ and CSZ-Al_2O_3--TiO_2 ceramic coatings. The following conclusions are drawn from this study:

– A single-layer CSZ coating and a double-layer CSZ-Al_2O_3-TiO_2 coatings are separately applied to Inconel X750 samples (two samples) using the air plasma spraying technique. The SEM image confirmed the presence of bond coat (NiCrAlY) and ceramic top coat CSZ and CSZ-Al_2O_3-TiO_2 on the substrate. More porosity is observed in the CSZ samples compared to the CSZ-Al_2O_3-TiO_2 sample. EDS ensures the presence of elements in the single layer and double layer coating.

– The XRD analysis of the CSZ samples shows the transformation of monoclinic to tetragonal ZrO_2 phases; this transformation is accompanied by large volume expansion occurring in the CSZ sample. Whereas the XRD analysis of CSZ-Al_2O_3-TiO_2 shows the phase transformation of alumina, there by the double layer coating possesses more phase stability.

– Raman spectroscopy has ascertained the states of various oxides present in the coating in the wavelength ranging from 109.24–378.36 cm^{-1} for the CSZ sample and in the wavelength ranging from 239–1048 cm^{-1} for the CSZ-Al_2O_3-TiO_2 sample.

– Double layer Al_2O_3-TiO_2 coated sample exhibits higher Vicker's micro hardness compared to the single layer CSZ coated sample. This is due to the fact that the lamellar distribution of Al_2O_3-TiO_2 reduces the surface defects thereby increasing the hardness during the sintering process.

– Hot corrosion studies reveal that the mass change per unit area of the single layer CSZ sample is observed as 18.66 mg cm^{-2} whereas that for CSZ-Al_2O_3-TiO_2 double layer coating is found to be 13.07 mg cm^{-2} under molten salt environment. It is evident that the CSZ sample under molten salt environment undergoes corrosion due to formation of cracks, pores and presence of some by products and presence of more amount of salt. Hence, it can be stated that, Al_2O_3-TiO_2 is more stable than CSZ in a molten environment.

– Based on the above results, CSZ-Al_2O_3-TiO_2 (Double layer Coating) has more susceptibility towards corrosion than CSZ (Single layer Coating) which aids to enhance its thermal life cycle.

Acknowledgements

The corresponding author sincerely acknowledges the Centre for Research (CFR), Anna University for providing financial support under the Anna Research Fellowship (ARF) scheme (CFR/ARF-July 2022/AR1/22142197185), which significantly contributed to the progress of this research. The author also expresses heartfelt thanks to E. Aswin Victor, PG student, Engineering Design Division, Anna University, for his constant support and valuable assistance throughout the study.

References

[1] H. Zhang, Y. Liu, X. Chen, H. Zhang, Y. Li, Microstructural homogenization and high-temperature cyclic oxidation behavior of a Ni-based superalloy with high Cr content, J. Alloys Compd. 727 (2017) 410–418. https://doi.org/10.1016/j.jallcom.2017.08.137

[2] D. Diwahar, V. Manivachakan, R. Begum Syed, An Overview of rare earth-doped ceramic thermal barrier coatings for high-temperature performance of nickel-based superalloys, High Temperature Corrosion of Mater. 102 (2025) 1–17. https://doi.org/10.1007/s11085-025-10340-8

[3] J. Li, J., Zhou, S. Zho, J. Sheng, The effect of cryogenic treatment on mechanical properties and microstructures of IN718 super alloy, Mater. Sci. Eng. A 5 (2017) 87–77. http://dx.doi.org/10.1016/j.msea.2017.09.049

[4] D. Diwahar, V. Manivachakan, R. B. Syed, S. K. Murugesan, A comprehensive study on CeO_2-Gd_2O_3 doped hydroxyapatite nano powders: Structural, optical, magnetic and biological properties insights for bone regeneration and osteosarcoma therapeutic applications, Mater. Chem. Phys. 350 (2025) 1–16. https://doi.org/10.1016/j.matchemphys.2025.131890

[5] A. Mesbahzade, S. H. Razavi, Z. Seyedraoufi, Y. Shajari, M. Samiee, Comparison of microstructure and adhesion strength of YSZ and MSZ thermal barrier coatings in the presence and absence of Al_2O_3 interface layer, J. Aust. Ceram. Soc. 59 (2023) 597–604. https://doi.org/10.1007/s41779-023-00856-0

[6] A. Avcı, M. Karabaş, A. Eker, E. Akman, Optimization of laser process parameters and improved corrosion behaviour of LZ/YSZ thermal barrier coating, J. Aust. Ceram. Soc. 61(2025) 1155–1171. https://doi.org/10.1007/s41779-025-01149-4

[7] R. Ran, Y. Wang, Y.-X. Zhang, F. Fang, Y.-K. Xia, W.-N. Zhang, G. Yuan, G.-D. Wang, Two-stage annealing treatment to uniformly refine the microstructure tailor δ precipitates and improve tensile properties of Inconel 718 alloy, J. Alloys Compd. 927 (2022) 66–88. https://doi.org/10.1016/j.jallcom.2022.166820

[8] J. Yu, D. Wang, J. Chen, C. Yang, X. Hao, J. Zhou, D. Li, D. Shu, C. Xiao ,Y. Peng, High temperature behaviors of a casting nickel-based superalloy used for 815 °C, Mater. 14 (2021) 702–716. https://doi.org/10.3390/ma14040716

[9] S. Maharajan, F. M. T. Rex, Microstructural characterization studies on hot corrosion behavior of YSZ/$Gd_2Zr_2O_7$ based plasma spray coatings on SS316, Phys. Scr. 100 (2024) 15–24. https://doi.org/10.1088/1402-4896/ad963d

[10] M. Bajt Leban, M. Vončina, T. Kosec, R. Tisu, M. Barborič, J. Medved, Comparison of cycling high temperature corrosion at 650 °C in the presence of NaCl of various austenitic stainless steels, High Temperature Corrosion of Mater. 99 (2023) 63–77. https://doi.org/10.1007/s11085-022-10138-y

[11] S. Tailor, N. Vashishtha, A. Modi, S. C. Modi, Microstructure evolution and mechanical properties

of Al_2O_3-40%TiO_2 coating by Hybrid-Low Velocity Oxyfuel process, Phys. Scr. 96 (2021) 025702. https://doi.org/10.1088/1402-4896/abce37
[12] C. Bartuli, L. Lusvarghi, T. Manfredini, T. Valente, Thermal spraying to coat traditional ceramic substrates: case studies, J. Eur. Ceram. Soc 27 (2007) 1615–1622. https://doi.org/10.1016/j.jeurceramsoc.2006.05.049
[13] Z. Chen, S. Speakman, J. Howe, H. Wang, W. Porter, R. Trice, Investigation of reactions between vanadium oxide and plasma-sprayed yttria-stabilized zirconia coatings, J. Eur. Ceram. Soc. 29 (2009) 1403–1411. https://doi.org/10.1016/j.jeurceramsoc.2008.09.016
[14] R. A. Miller, Current status of thermal barrier coatings – An overview, Surf. Coat. Technol. 30 (1987) 1–11. https://doi.org/10.1016/0257-8972(87)90003-X
[15] G. Sreedhar, M. D. Masroor Alam, V. S. Raja, Hot corrosion behaviour of plasma sprayed YSZ/Al_2O_3 dispersed NiCrAlY coatings on Inconel-718 superalloy, Surf. Coat. Technol. 3 (2009) 291–299. https://doi.org/10.1016/j.surfcoat.2009.07.026
[16] H. Hayashi, M. Kanoh, C. J. Quan, H. Inaba, S. Wang, M. Dokiya, H. Tagawa, Thermal expansion of Gd-doped ceria and reduced ceria, Solid State Ion. 132 (2000) 227–233. https://doi.org/10.1016/S0167-2738(00)00646-9
[17] S. Hong, J. Lin, Y. Wu, J. Wu, Y. Zheng, Y. Zhang, J. Cheng, W. Sun, Cavitation erosion characteristics at various flow velocities in NaCl medium of carbide-based cermet coatings prepared by HVOF spraying, Ceram. Int. 47 (2021) 1929–1939. https://doi.org/10.1016/j.ceramint.2020.09.022
[18] Q. M. Yu, L. Cen Y. Wang, Numerical study of residual stress and crack nucleation in thermal barrier coating system with plane model, Ceram. Int. 44 (2018) 51116–5123. https://doi.org/10.1016/j.ceramint.2017.12.112
[19] E. P. Busso, Z. Q. Qian, M. P. Taylor, H. E. Evans, The influence of bond coat and topcoat mechanical properties on stress development in thermal barrier coating systems, Acta Mater. 57 (2009) 2349–2361. https://doi.org/10.1016/j.actamat.2009.01.017
[20] R. A. Miller, C. E. Lowell, Failure mechanism of thermal barrier coatings exposed to elevated temperature, Thin Solid Films 95 (1982) 265–273. https://doi.org/10.1016/0040-6090(82)90019-0
[21] D. R. Clarke, C. G. Levi, Materials design for the next generation thermal barrier coatings, Annual Review of Materials Research 33 (2003) 383–417. https://doi.org/10.1146/annurev.matsci.33.011403.113718
[22] A. Moridi, M. Azadi, G. H. Farrahi, Thermo-mechanical stress analysis of thermal barrier coating system considering thickness and roughness effects, Surf. Coat. Technol. 243 (2014) 91–99. https://doi.org/10.1016/j.surfcoat.2012.02.019
[23] F. Vargas, E. López, H. Ageorges, Wear behavior at high temperature of ZrO_2–Y_2O_3 (YSZ) plasma-sprayed coatings, J. Mater. Sci. 6 (2023) 77–89. https://doi.org/10.1007/s10853-023-09204-w
[24] S. Limbu, Investigation of crystal structure confinement and optical attributes of monoclinic–tetragonal Zirconia nanocrystals via chemical co-precipitation technique, Bull. Mater. Sci. 45 (2022) 182. https://doi.org/10.1007/s12034-022-02769-3
[25] G. M. Ingo, T. De Caro, Chemical aspects of plasma spraying of zirconia-based thermal barrier coatings, Acta Mater. 56 (2008) 5177–5187. https://doi.org/10.1016/j.actamat.2008.07.006
[26] S. Y. Park, J. H. Kim, M. C. Kim, H. S. Song, C. G. Park, Microscopic observation of degradation behavior in yttria and ceria stabilized zirconia thermal barrier coatings under hot corrosion, Surf. Coat. Technol. 190 (2005) 357–365. https://doi.org/10.1016/j.surfcoat.2004.04.065
[27] K. Lakshmi, M. C. Rao, V. Dubey, Structural and thermoluminescence glow curve analysis of Eu^{3+}-doped $LaCePO_4$ phosphor, J. Russ. Phys. 67(2024) 993–999. https://doi.org/10.1007/s11182-024-03208-y
[28] M. Ritz, M. Valášková, Infrared and Raman spectroscopy of three commercial vermiculites doped with cerium dioxide nanoparticles, Spectrochim, Acta A Mol. Biomol. Spectrosc. 201 (2018) 39–45. https://doi.org/10.1016/j.saa.2018.04.053
[29] D. W. Wheeler, J. Zekonyte, R. J. K. Wood, Structure and mechanical properties of Ce-La alloys containing 3–10 wt.% La, J. Nucl. Mater. 543 (2021) 52–49. https://doi.org/10.1016/j.jnucmat.2020.152497
[30] M.-F. Luo, P. Fang, M. He, Y.-L. Xie, In situ XRD, Raman, and TPR studies of CuO/Al_2O_3 catalysts for CO oxidation, J. Mol. Catal. A: Chem. 239 (2005) 243–248. https://doi.org/10.1016/j.molcata.2005.06.029
[31] S. N. Dub, G. A. Gogotsi, E. E. Lomonova, Hardness and fracture toughness of tetragonal zirconia single crystals, J Mater Sci Lett. 14 (1995) 46–49. https://doi.org/10.1007/BF02565283
[32] S. M. Hashemi, N. Parvin, Z. Valefi, Effect of addition of multimodal YSZ and SiC powders on the mechanical properties of nanostructured Cr_2O_3 plasma-sprayed coatings, Therm Spray Tech. 28 (2019) 544–562. https://doi.org/10.1007/s11666-019-00834-8
[33] L. Li, L. Li, G. Zhang, H. Xu, M. Cui, W. Wang, D. Liu, Hot Corrosion Behavior of Inconel 625 in Na_2SO_4 and V_2O_5 Molten Salt System, Metals 13 (2023) 1069. https://doi.org/10.3390/met13061069
[34] F. Duarte Martinez, A. Syed, K. Dawson, G. J. Tatlock, N. I. Morar, M. Kothari, G. M. Castelluccio, Effect of NaCl and SO_2 on stress corrosion cracking of CMSX-54 AT 550 °C, Mat. High Temp. 40 (2023) 283–295. https://doi.org/10.1080/09603409.2023.2205760
[35] B. Mousavi, M. Farvizi, M. R. Rahimipour, W. Pan, Comparison of the hot corrosion behavior of the LZ, CSZ and LZ/CSZ composite thermal barrier coating, Surf. Coat. Technol. 437 (2022) 25–28. https://doi.org/10.1016/j.surfcoat.2022.128324
[36] M. Nejati, M. R. Rahimipour, I. Mobasherpour, Evaluation of hot corrosion behaviour of CSZ, CSZ/micro Al_2O_3 and CSZ/nano Al_2O_3 plasma sprayed thermal barrier coatings, Ceram. Int. 40 (2014) 79–90. https://doi.org/10.1016/j.ceramint.2013.08.135
[37] A. Shamsini, M. Saremi, M. H. Sohi, Oxidation and hot corrosion characteristics of YSZ/ NiCoCrAlY electrophoretically deposited on IN-738, J. Mater. Res. Technol. 41 (2026) 1193–1203. https://doi.org/10.1016/j.jmrt.2025.12.067
[38] D. Shi, J. Song, S. Li, H. Qi, X. Yang, Cracking behaviours of EB-PVD thermal barrier coating under temperature gradient, Ceram. Int.15 (2019) 18–28. https://doi.org/10.1016/j.ceramint.2019.06.071